Solid-state compatibility of Ca:LaNbO₄ with perovskite cathodes: evidences from X-ray microspectroscopy

Alessandro Chiara[1], Giovanna Canu[2], Alessandro Longo[3,4], Candida Pipitone[1], Antonino Martorana[1] and Francesco Giannici[1,*]

1 Dipartimento di Fisica e Chimica "Emilio Segrè", Università di Palermo, Viale delle Scienze 90128, Palermo, Italy

2 CNR-ICMATE – Institute of Condensed Matter Chemistry and Technologies for Energy, Via De Marini 6, 16149, Genova, Italy

3 ISMN-CNR - Istituto per lo Studio Dei Materiali Nanostrutturati, Via Ugo La Malfa, 153, 90146, Palermo, Italy

4 European Synchrotron Radiation Facility, 71, Avenue des Martyrs, Grenoble, F-38000, France

* to whom correspondence should be addressed: francesco.giannici@unipa.it

Abstract

The solid-state compatibility between calcium-doped lanthanum niobate and three perovskite cathode materials was investigated using two X-ray microbeam techniques, micro X-ray fluorescence and micro X-ray absorption spectroscopy. The cathode powders (lanthanum strontium ferrite, either cobalt or copper-doped, and lanthanum strontium cobaltite) in contact with the dense electrolyte pellet were annealed at 1150 °C for 12-144 hours to simulate the effect of thermal stresses due to fabrication and long-term operation. As a result, several interdiffusion phenomena were then observed on the bilayer cross-sections: in particular, the chemical state and coordination environment of calcium, iron, niobium and lanthanum were probed with space-resolved X-ray absorption spectroscopy. The ab initio modeling of the near-edge X-ray absorption spectra reveal that the cation interdiffusion is facilitated by the structural flexibility of the perovskite structure, which is able to accommodate a variety of foreign cations in different oxidation states. Limited stability at high-temperatures was found for all candidate perovskite compositions in contact with lanthanum niobate.

1. Introduction

For decades, energy production and conversion have been at the forefront of materials research, propelled by the ever-increasing need to generate and store electrical power by more efficient and environmentally friendly processes. In this context, solid-oxide cells convert hydrogen to electricity or *vice versa* when working in fuel cell and electrolyzer modes, making them a central device in the envisioned hydrogen economy. Among electrolytes for solid-oxide cells, proton conductors have a few decisive advantages with respect to oxygen conductors, especially in the intermediate-temperature range (around 600 °C), because of the lower activation energy of the ion conduction process. [1–3] They also have advantages in device operation: water is formed at the cathode side, avoiding the dilution of the fuel. High proton conductivity is found in perovskites, especially barium cerates and zirconates, whose crystallochemical and electrochemical properties have been extensively investigated in the last decades. [4,5] Despite their appealing conductivity, those perovskites have either poor grain boundary conductivity ($BaZrO_3$) or limited chemical stability to CO_2 ($BaCeO_3$): [6,7] even when the composition of cerates/zirconates is engineered to overcome the above issues, their chemical compatibility with the most common ceramic cathodes is less than ideal [8–13].

The most studied alternative to perovskite-based proton conductors is $LaNbO_4$, extensively studied as a SOFC electrolyte by Norby's group in Oslo [14]. To increase proton concentration and consequently proton conductivity, doping of the lanthanum site with a divalent dopant (e.g., Ca^{2+}) is usually performed. In general, the flexibility of the $LaNbO_4$ lattice is fairly low so that the resulting dopant solubility is limited to 1-2% mol.

The compatibility of lanthanum niobates with ceramic cathode materials was rarely investigated, with electron microscopy and X-ray diffraction [15–17], or with impedance spectroscopy [18], showing no reactivity with $LaMnO_3$ or $LaFeO_3$, and the formation of secondary phases in contact with cobalt- or nickel-containing cathodes. Only two X-ray microspectroscopy studies exist in the literature, highlighting the intrinsic tendency of Ca or W dopants to exsolve from the parent $LaNbO_4$ lattice in contact with $(La,Sr)MnO_3$. [19,20] In any case, recent research efforts on lanthanum niobate attest to an ongoing interest in non-perovskite materials as potential SOFC electrolytes [16,20–25], warranting a more comprehensive understanding of its chemical compatibility in the solid-state.

In this paper, we investigate the microstructure and chemical composition of the interface of $La_{0.98}Ca_{0.02}NbO_4$ (LNC) electrolyte after prolonged contact at high temperature with three different cathode perovskites materials: $La_{0.6}Sr_{0.4}Fe_{0.8}Cu_{0.2}O_3$ (LSFCu),

$La_{0.6}Sr_{0.4}Fe_{0.85}Co_{0.15}O_3$ (LSCF) and $La_{0.6}Sr_{0.4}CoO_3$ (LSC). The cathode/electrolyte interfaces were studied by scanning X-ray microspectroscopy and X-ray absorption near edge structure (XANES) using a synchrotron microbeam. The obtained results attest to the limited stability of the LNC/cathode interface when annealed at high temperature with the investigated cathodes due to the formation of secondary phases with various compositions and morphologies. Our study highlights the importance of chemical compatibility between cathode and electrolyte, especially in the high-temperature regime. Moreover, it highlights the necessity of a better understanding of the finer solid-state phenomena at the interface to maximize materials compatibility in the long term. [8]

2. Experimental section

LSCF and LSC powders (Marion Technologies) were used as received, while LSFCu and LNC were synthetized by combustion synthesis and solid-state reaction, respectively. Phase purity was assessed by X-ray powder diffraction.

The cathode/electrolyte bilayers, comprising a LNC dense pellet surrounded by cathode powder, were heat treated at 1150°C for either 12, 72, or 144 hours. The annealed cathode/electrolyte couples were embedded in epoxy resin, cross-cut, and polished to expose the cathode/electrolyte interface.

Scanning X-ray microspectroscopy was carried out at beamline ID21 of the European Synchrotron Radiation Facility, Grenoble, France [26], at the Nb L_3-edge (2.4 keV), Ca K-edge (4.0 keV), La L_3-edge (5.5 keV), and Fe K-edge (7.2 keV). The beam size was 450-750 nm x 400-450 nm (H x V), with a photon flux between 1 and 3 x 10^{10} ph/s, depending on the beam energy. Data reduction and concentration maps were obtained with PyMca [27] using the Spectrocrunch package. [28] Fully relativistic electronic structure calculations were carried out with FDMNES to simulate the XANES spectra using the finite difference method [29,30]. As often happens with ionic materials, the non-excited absorbing atom, screening, and dilatorb approximations/corrections were used in the *ab initio* calculation to obtain the best agreement between simulated and measured spectra. Further details on materials preparation and measurement geometry, resolution, and data analysis are found in Ref. [12,19,31].

3. Results and discussions

3.1 LSFCu/LNC

A substantial reaction is observed in the LSFCu/LNC couple after 12 hours of aging: a wide reactivity zone, larger than 50 μm, is visible in the concentration profiles (Figure 1) and even more evident in the elemental maps (Figure 2).
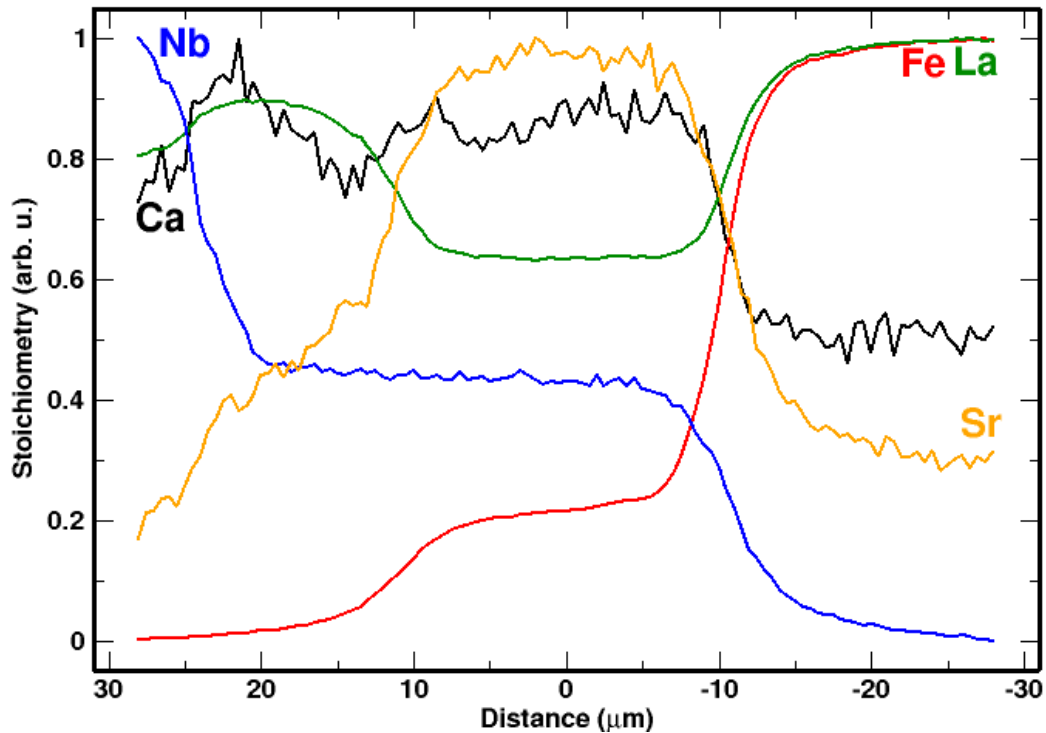

Figure 1 - LSFCu/LNC 12 h at the Fe K-edge. Concentration profiles of niobium (blue), calcium (black), lanthanum (green), iron (red), and strontium (orange).

 A closer inspection reveals the formation of two distinct secondary phases: one is closer to the cathode side, and it is enriched in strontium, calcium and iron, and depleted in lanthanum; the other phase is formed at the electrolyte side, and it is mainly composed of lanthanum and calcium, and secondarily of strontium. The niobium content is almost constant throughout the reaction zone and substantially lower compared to the LNC stoichiometry.
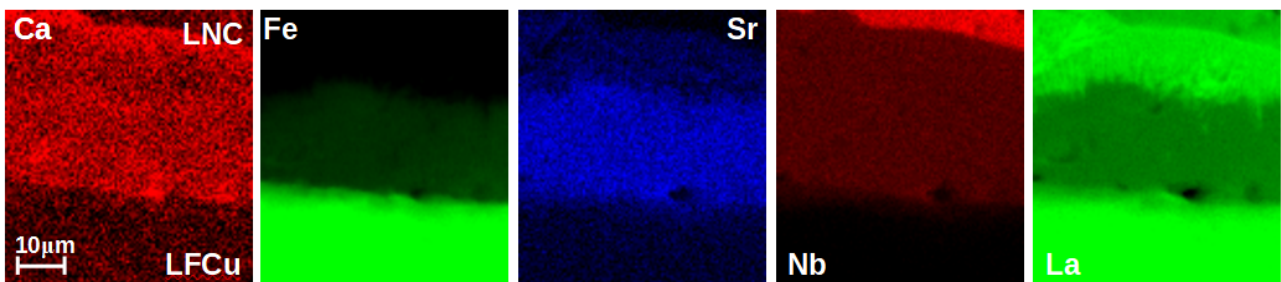
Figure 2 - LSFCu/LNC 12 h at the Fe K-edge. Left to right: concentration maps of calcium (red), iron (green), strontium (blue), niobium (red), lanthanum (green).

Figure 3 shows the concentration profiles after 72 hours of annealing. In these profiles, the wide reaction layer (> 150 μm) is much sharper and evident. The sharp peaks in the calcium profile on the far left are due to the localized buildup of calcium in bulk LNC, already described in Ref. [19].
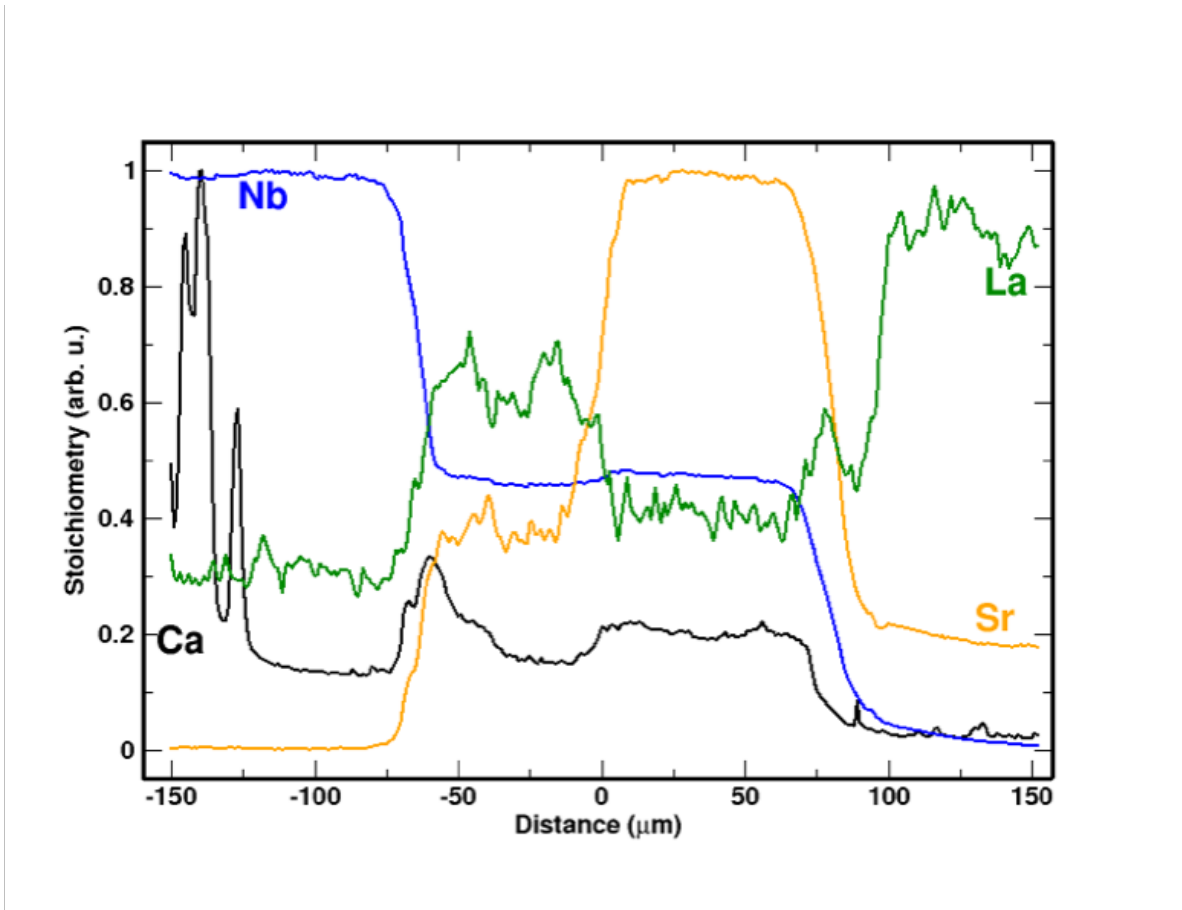

Figure 3 - LSFCu/LNC 72 h at the Ca K-edge. Concentration profiles of niobium (blue), calcium (black), strontium (orange) ad lanthanum (green).

Because of the extensive reaction zone, the microXRF mapping of this sample is carried out by tiling three different maps together across the interface, as shown in Figure 4. The cations profiles here suggest the formation of three different secondary phases, layered on top of each other and parallel to the interface. In these regions, niobium concentration is almost constant, while other elements accumulate. In particular, a thin layer enriched in calcium is formed closest to LNC (at around -60 μm in Figure 3); moving towards the cathode side, a second layer is formed, appearing as a heterogeneous aggregate of tiny particles with

variable composition (but relatively depleted in calcium). The second layer is most likely the product of cation diffusion alongside meandering grain boundaries. Eventually, one last layer around 100 μm thick can be observed: it is highly enriched in strontium (coming from the cathode) and depleted in lanthanum.
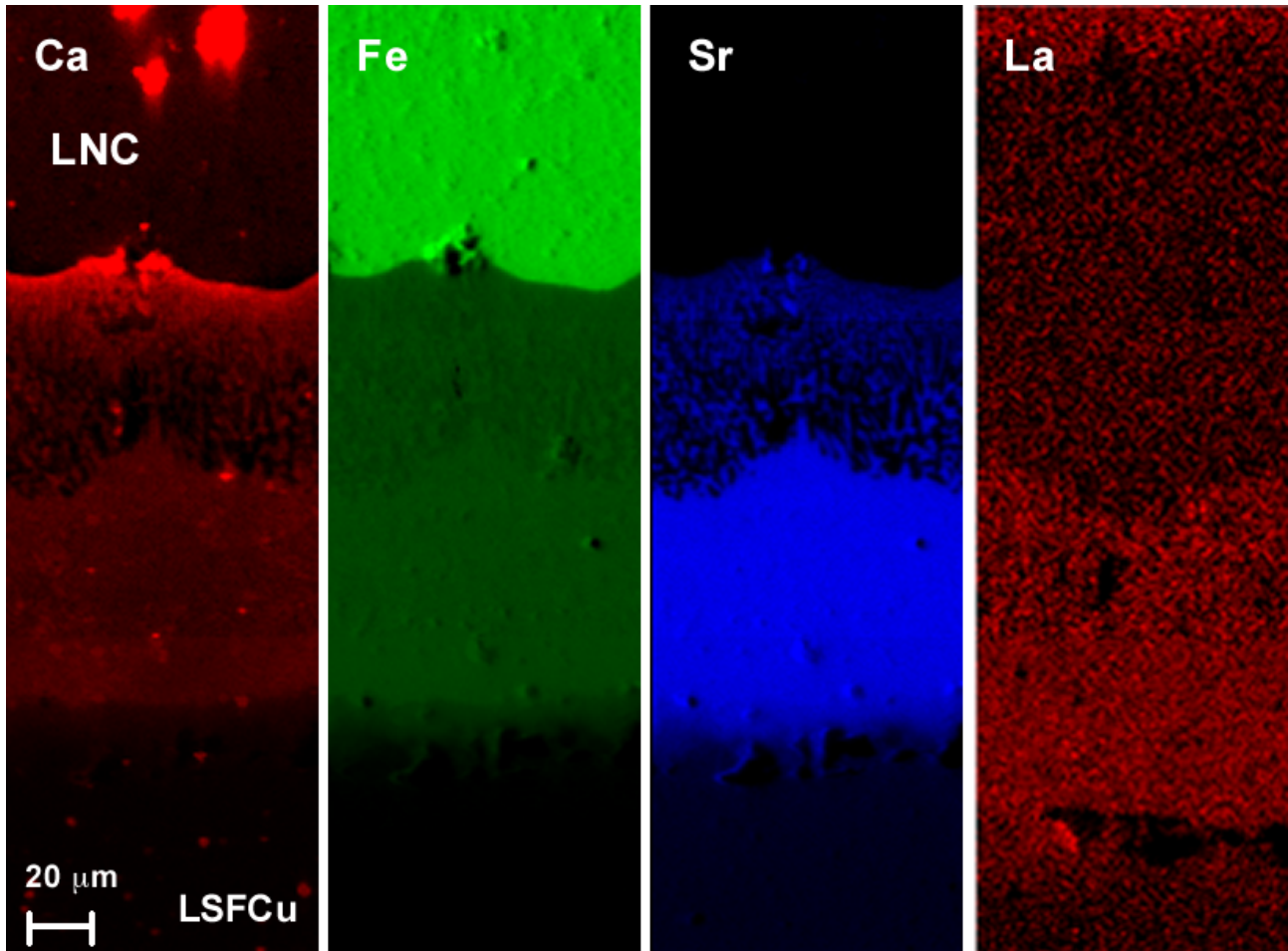

Figure 4 - LSFCu/LNC 72 h at the Ca K-edge. Left to right: concentration maps of calcium (red), niobium (green), strontium (blue) and lanthanum (red).

From the above results, a strong reactivity between LSFCu and LNC is evident at 1150 °C. MicroXANES spectra at both Ca and Fe K-edges provide valuable hints for identifying the products of such reactions. The layer closest to LSFCu is recognized as an accumulation of strontium in a perovskite containing Sr, La and Ca in the A-site, much enriched in strontium than the pristine LSFCu phase. Fe K-edge spectra, shown in Figure 5, always feature Fe in a perovskite local environment, with varying absorption edge energy due to Fe^{3+}/Fe^{4+} variable valence. In particular, the edge shifts to higher energy (increasing valence) in the Sr-enriched zone. The integrated intensity of the Sr emission line in the spots shown in Figure 5 increases about five times between spots 1 (LSFCu) and 5 (LNC). In the last spot,

due to the Sr^{2+} enrichment, the perovskite Fe cation has a higher valence than in LSFCu (formally +3.2).
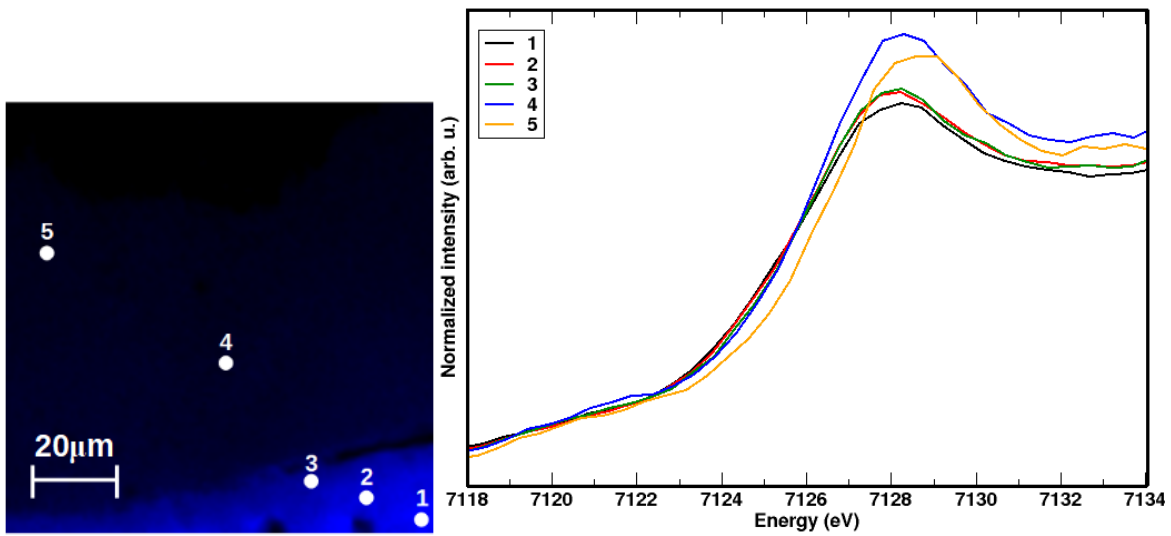

Figure 5 - LSFCu/LNC 72 h at the Fe K-edge. (Left) concentration map of iron (blue). (Right) Fe K-edge microXANES spectra measured at the different points whose position relative to the interface is shown in the left panel.
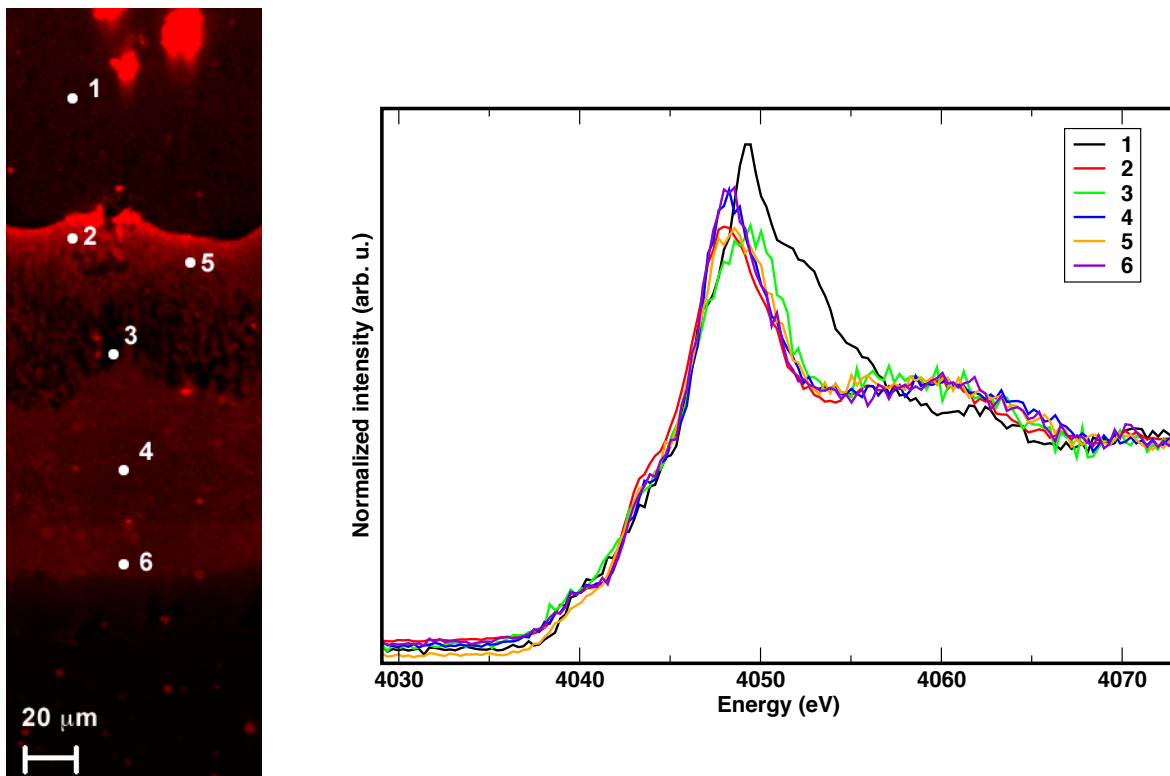

Figure 6 - LSFCu/LNC 72 h at the Ca K-edge. (Left) concentration map of calcium (red). (Right) Ca K-edge microXANES spectra measured at different points shown in the left panel.

The analysis of Ca K-edge spectra (Figure 6) allows identifying the other Ca-containing phases closer to the LNC side. Spot 1 in Figure 6 is measured inside LNC, while the other spots are measured in different regions inside the reaction zone. The latter spectra are very different from Ca in LNC and can be substantially modeled by *ab initio* simulations, shown in Figure 7. Simulated spectra indeed confirm the chemical environment of the distorted eightfold coordination of Ca^{2+} substituting La^{3+} in the LNC lattice. In contrast, the spectrum acquired in the layer close to the LNC side (spot 2), rich in calcium and niobium, can be identified as a mixture of $(Ca,Sr)_2Nb_2O_7$ and $CaCO_3$. $Sr_2Nb_2O_7$ was previously hypothesized as a secondary phase in Sr-doped $LaNbO_4$ ceramics treated at high temperatures. Therefore a similar compound is not unexpected in LNC [32,33]. It is worth noting that although calcium in LNC has long been assumed to substitute La^{3+} in bulk $LaNbO_4$ [14], this is the first direct evidence of its incorporation in the LNC lattice. Calcium exsolution from LNC [19] due to its low solubility [32], and the high mobility of strontium from cathode perovskite materials has been extensively described in the literature. [34,35]
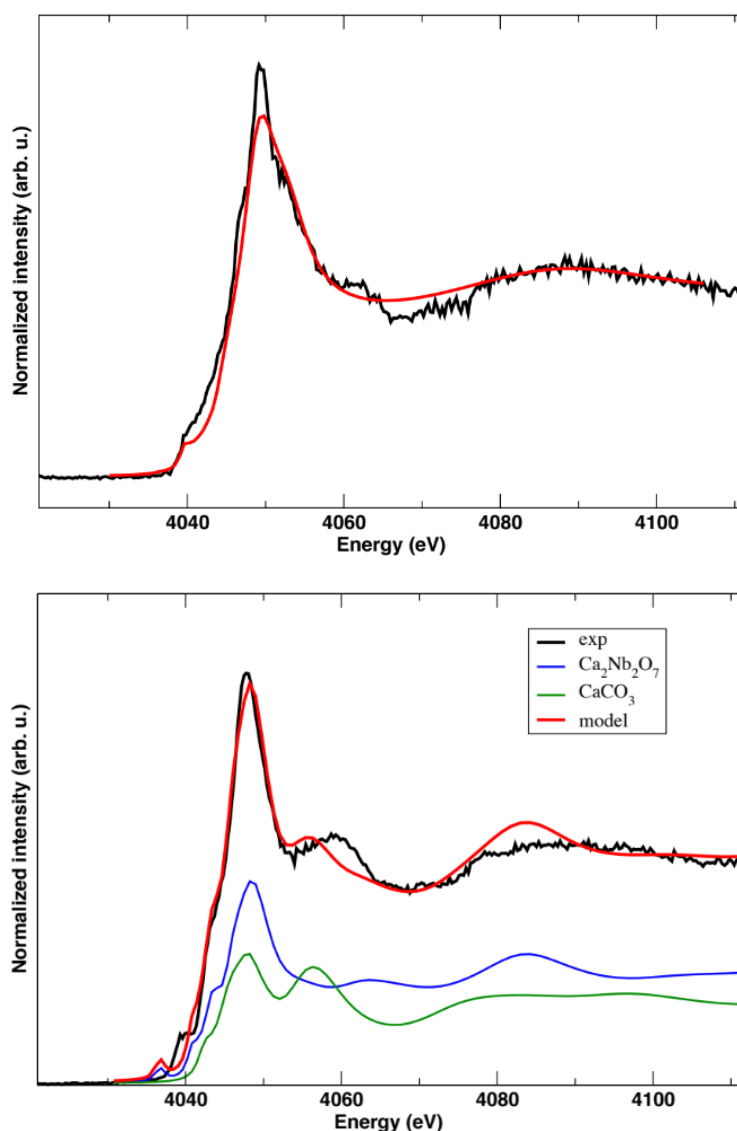
Figure 7 – LSFCu/LNC 72 h. Ca K-edge microXANES spectra (black) measured in spot 1 (bulk LNC, top panel) and spot 2 (interface, bottom panel) together with the modeled spectra (red): the modeled spectra are calculated for Ca^{2+} in the La-site of LNC in spot 1, and a mixture of $Ca_2Nb_2O_7$ (blue) and $CaCO_3$ (green) in spot 2.

Adding a significant fraction of calcium in a $CaCO_3$ environment (around 40-50%) is necessary to achieve a satisfactory agreement between data and the model in the bottom panel, especially around 4050-4060 eV. The Sr solubility in $CaCO_3$ is very low [36,37], so all the Sr detected in this region is expected to be incorporated into the $(Ca,Sr)_2Nb_2O_7$ layered perovskite. In spot 3, the calcium local environment resembles a mixture of LNC and $Ca_2Nb_2O_7$, with the main edge slightly shifted to higher energy. At this point, niobium and lanthanum dominate the composition at the expense of strontium, so the recrystallization of lanthanum niobate seems plausible.

While LNC is stable against carbonation [18], it is possible that after the exsolution of calcium, some CaO in tiny domains is eventually carbonated. However, we cannot rule out that a different unidentified Ca-containing species is present, with a very similar local environment as in $CaCO_3$ to reproduce the distinctive spectral feature at 4060 eV.

3.2) LSCF/LNC

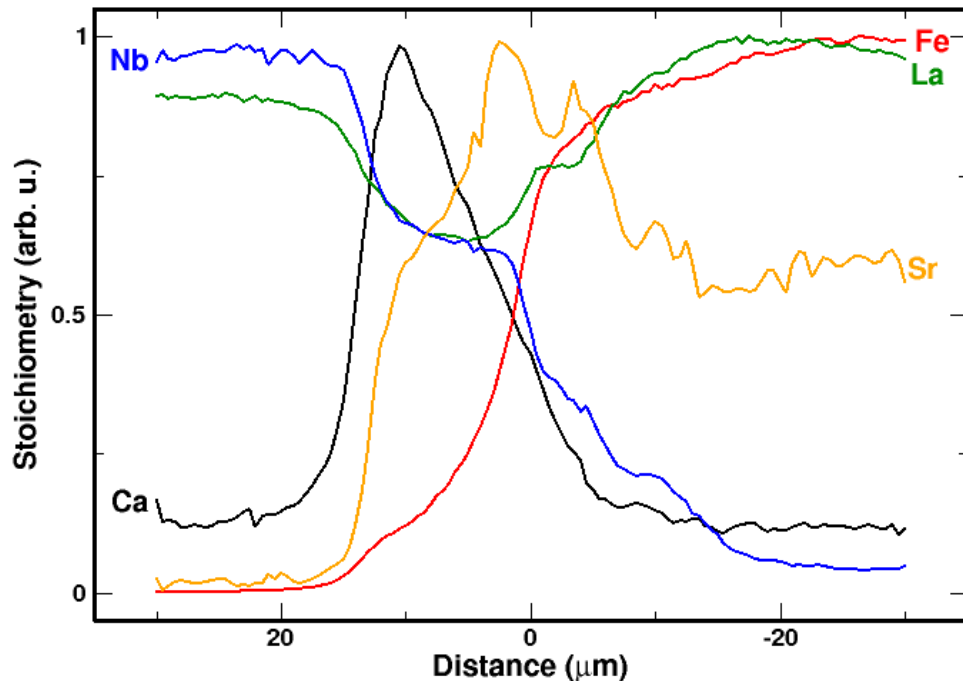The cations profiles of LSCF/LNC acquired at Fe K-edge are shown in Figure 8.

Figure 8 - LSCF/LNC 144 h at the Fe K-edge. Concentration profiles of niobium (blue), calcium (black), lanthanum (green), iron (red), and strontium (orange).

The LSCF/LNC couple shows much less conspicuous reactivity than LSFCu/LNC, although a clearly defined reactivity zone 30 μm wide is visible after 144 hours of aging.

In this case, different interfacial layers can be identified in the maps, shown in Figure 9. All cations diffuse towards the opposing side to a variable extent, so all layers inside the reactivity zone contain a significant fraction of all cations. Close to the LNC side, there is a stark accumulation of calcium at the expense of both lanthanum and niobium, and a significant amount of strontium is also present.

On the LSCF side, strontium is even more enriched, always at the expense of lanthanum: the most likely product is a mixed $(La,Sr,Ca)(Co,Fe,Nb)O_3$ perovskite with a high Sr content. The LNC side phase is rich in calcium and niobium, and deficient in lanthanum. Also in this case, this secondary phase can be identified as $(Ca,Sr)_2Nb_2O_7$ from the analysis of the Ca K-edge spectra discussed below.
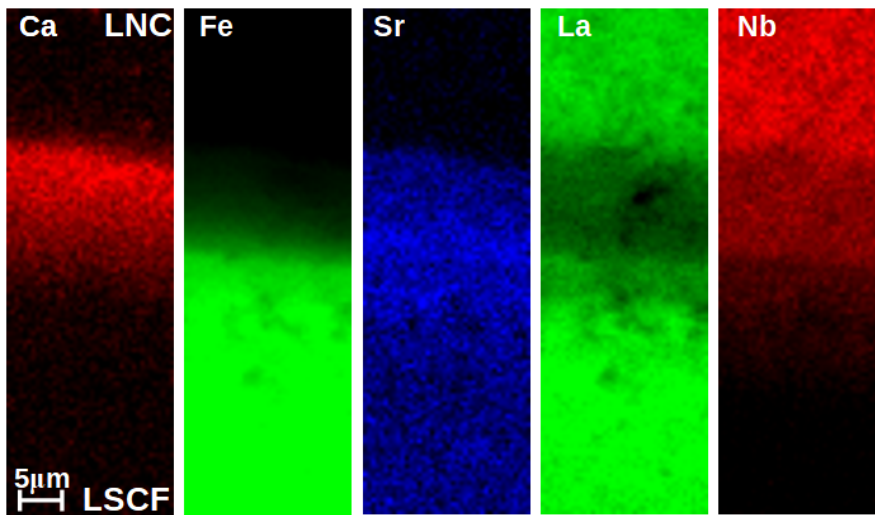
Figure 9 - LSCF/LNC 144 h at the Fe K-edge. Left to right: concentration maps of calcium (red), iron (green), strontium (blue), lanthanum (green) and niobium (red).

The microXANES spectra recorded at the Fe K-edge are reported in Figure 10. Once more, the absorption edge overall shape and edge features are maintained, demonstrating that iron is always incorporated in the B-site of a perovskite structure. However, the edge energy shifts significantly to the right as the iron average valence is changed from +3.2 in the parent LSCF phase (spots 1-3) to about +3.6 in a Sr-enriched perovskite in the reaction zone (spot 7).
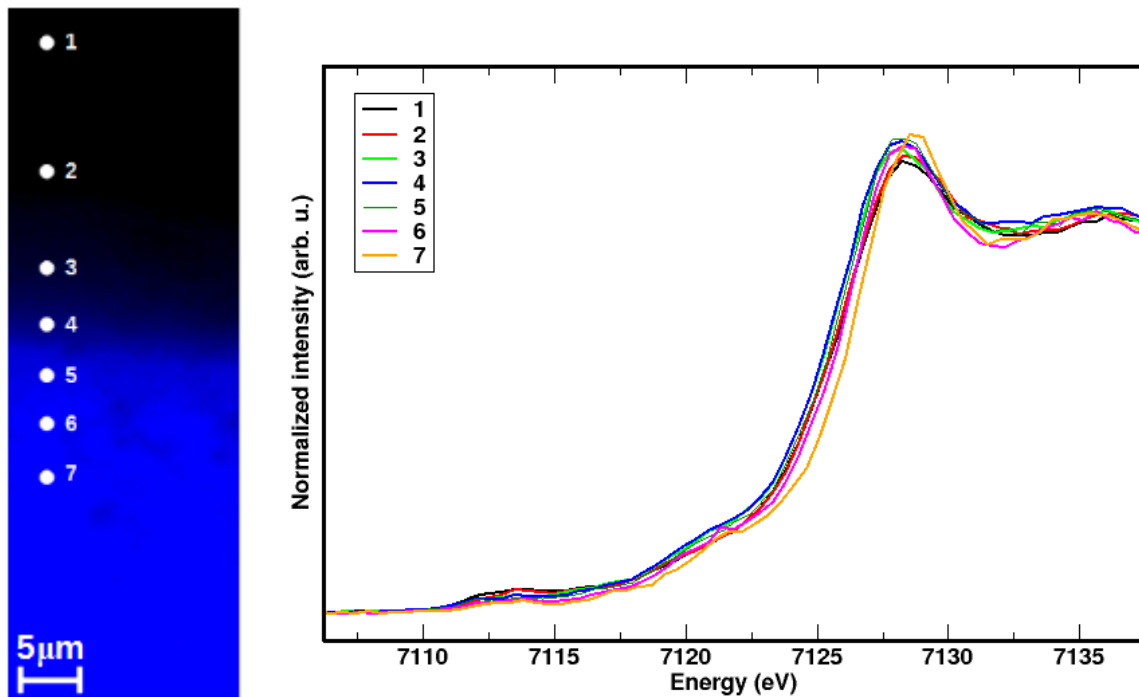
Figure 10 - LSCF/LNC 144 h at the Fe K-edge. (Left) concentration map of iron (blue). (Right) Fe K-edge microXANES spectra measured at different points shown in the left panel.
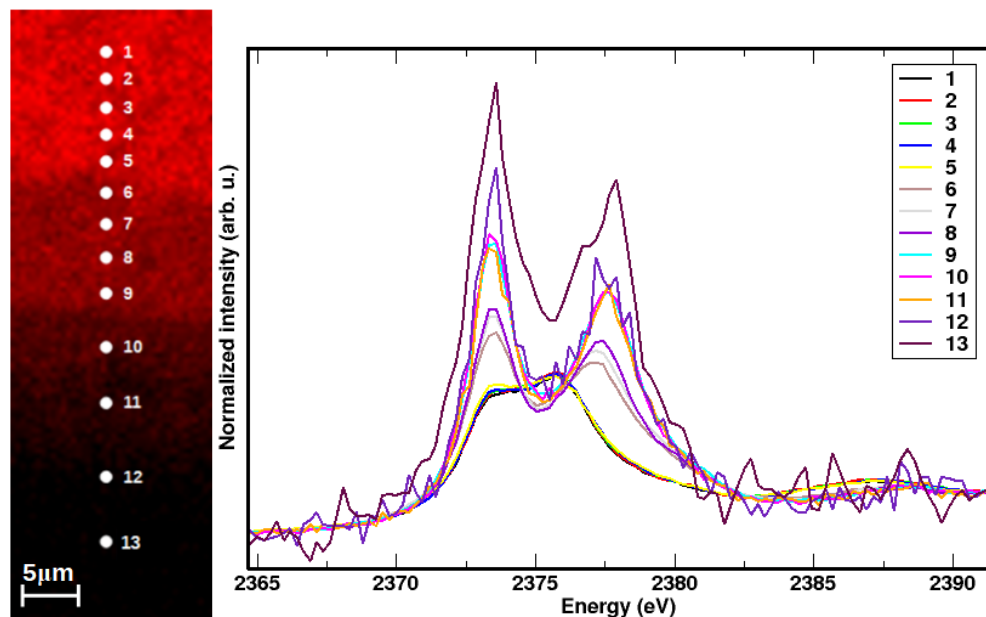

Figure 11 - LSCF/LNC 144 h at the Nb L_3-edge. (Left) concentration map of niobium (red). (Right) Nb L_3-edge microXANES spectra measured at different points shown in the left panel.

The spectra recorded at the Nb K-edge are reported in Figure 11. The absorption edge features change dramatically when moving across the interface, testifying to a change of local environment for niobium, from LNC to the reactivity layers, and eventually inside LSCF. The *ab initio* simulations once more help to identify unambiguously the niobium local environment. Inside bulk LNC, niobium is as expected Nb^{5+} in a tetrahedral coordination (see below for an analogous fitting). When diffusing towards the reaction layers, the main absorption edge splits in two peaks, typical of the perovskite local octahedral environment [19]. In particular, pentavalent niobium in the layered perovskite structure $Ca_2Nb_2O_7$ (Figure 12 (top)) reproduces well the experimental spectra in the reaction layer, spots 6 and 7 of Figure 11. Further inside the cathode region, niobium is still detectable in an appreciable amount, and here the spectra change even more. In spot 13, there is not enough calcium to form $Ca_2Nb_2O_7$, consequently, Nb^{5+} is incorporated in the B-site of LSCF (Figure 12 (bottom)). The tendency for Nb^{5+} to be incorporated in the perovskite lattice (in the absence of calcium) is in line with the eventual formation of the $LaCo_{2/3}Nb_{1/3}O_3$ ordered perovskite reported in $LaNbO_4/LaCoO_3$ diffusion couples [15].
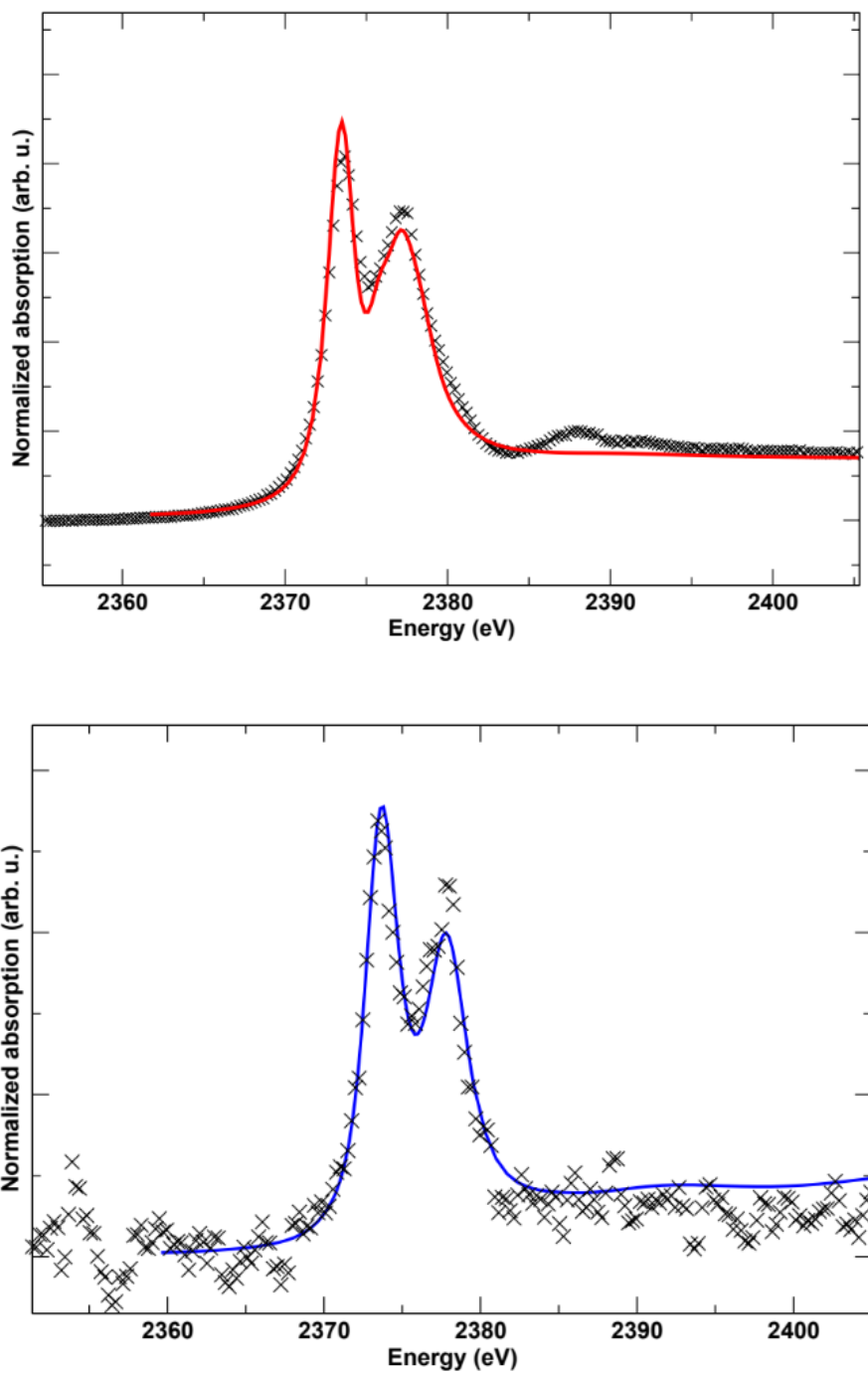
Figure 12 – LSCF/LNC 144 h. Nb L_3-edge microXANES spectra (crosses) measured in spot 6 (top) and spot 13 (bottom) together with the modeled spectra (lines): the modeled spectra are calculated for Nb^{5+} in $Ca_2Nb_2O_7$ and Nb^{5+} in the B-site of LSCF, respectively.
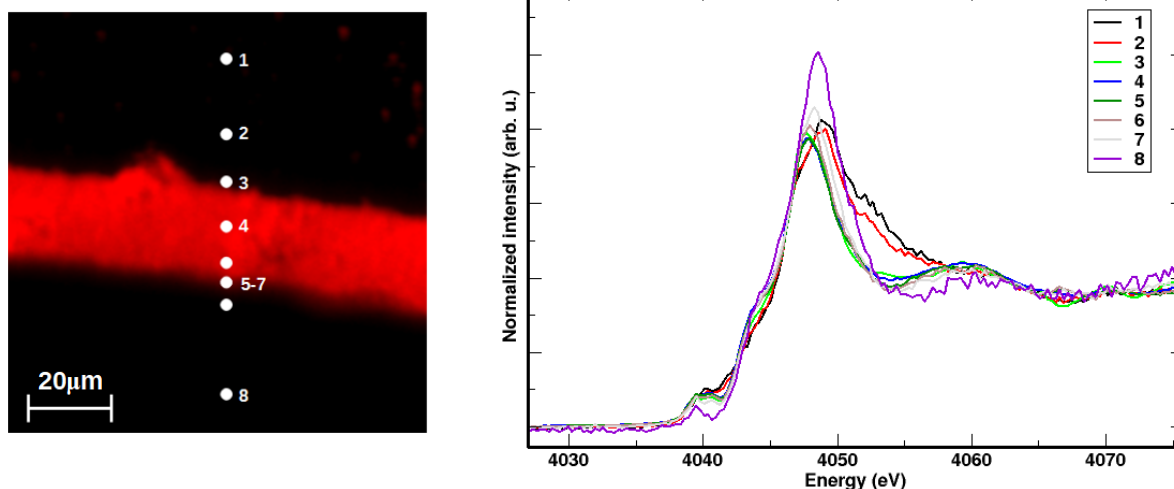
Figure 13 - LSCF/LNC 144 h at the Ca K-edge. (Left) concentration map of calcium (red). In this panel, LNC is on top, and LSCF is on the bottom. (Right) Ca K-edge microXANES spectra measured at the different points in the bulk and across the interface shown in the left panel.

The spectra recorded at the Ca K-edge across the LSCF/LNC interface are reported in Figure 13. Also, at calcium K-edge, the microXANES spectra suggest three different local environments in the different zones across the interface, confirmed by the *ab initio* simulation (Figure 14). In particular, in the bulk of LNC (spots 1 and 2 of Figure 13) the local environment of Ca^{2+} is correctly modeled by the distorted 8-fold coordination of the low-temperature fergusonite $LaNbO_4$ structure. Spots 3 to 6 feature a different local environment, whose sharp white line is well modeled with a $Ca_2Nb_2O_7$ layered perovskite environment. The second bump around 4060 eV can be reproduced by assuming a significant fraction of Ca^{2+} (around 15-20%) sits in a secondary phase with the $CaCO_3$ structure. In spot 8, the spectrum can be modeled using the LSCF structure, with Ca^{2+} in the perovskite A-site.
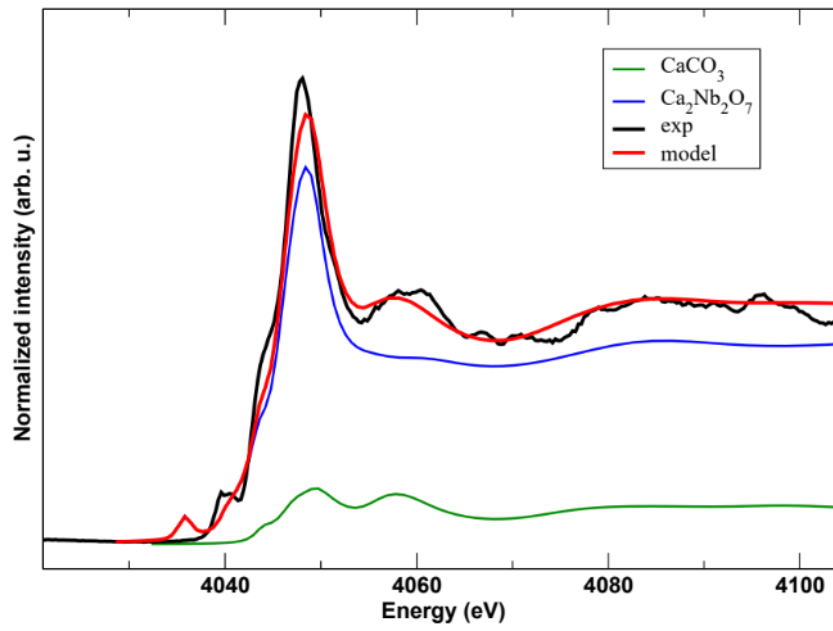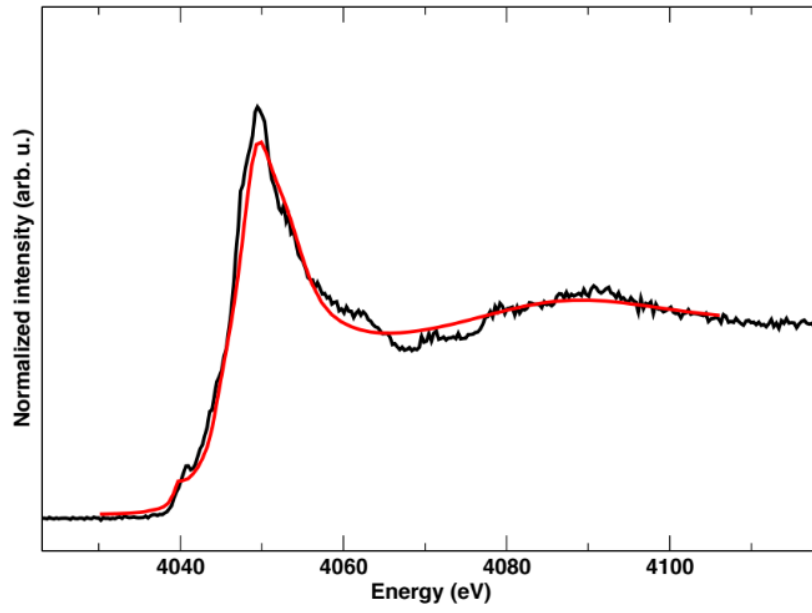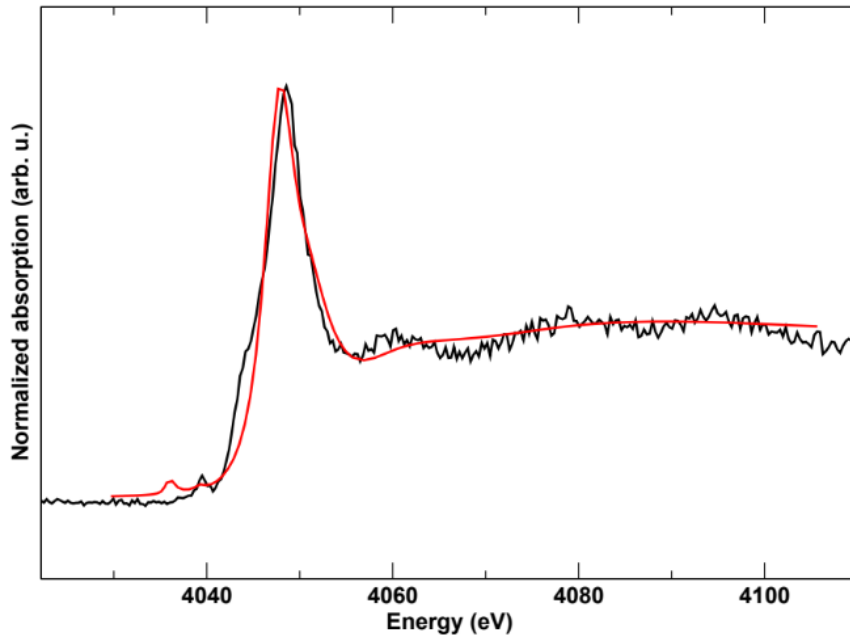
Figure 14 – LSCF/LNC 144 h. Ca K-edge microXANES spectra (black) measured in spot 1 (top), spot 5 (middle), and spot 8 (bottom) together with the modeled spectra (red): the modeled spectra are calculated for Ca^{2+} in the La-site of LNC (in spot 1), a mixture of $Ca_2Nb_2O_7$ plus $CaCO_3$ (in spot 5), and Ca^{2+} in the La-site of LSCF (in spot 8).

A striking similarity is evident in the secondary phases formed at the interface from comparing microXANES spectra of LSFCu/LNC and LSCF/LNC. In both cases, Ca^{2+} exsolved from LNC is not completely incorporated in a perovskite-like phase. However, it forms some extremely dispersed $CaCO_3$ phase in various concentrations, whose spectroscopic signature at 4060 eV is of clear assignment.

From the evidence of high reactivity found for both LSFCu/LNC and LSCF/LNC couples and from the prior reported stability of a $LaNbO_4/LaFeO_3$ couple [15], it can be inferred that both copper and cobalt are responsible for the increase of reactivity. Anyway, It should be noted that undoped materials are undoubtedly more stable from a solid-state chemical point of view but generally not suitable for practical applications.

3.3. LSC/LNC

The interface between LSC and LNC after annealing shows a very complex pattern of intergrown secondary phases. The concentration profiles and maps for this electrode/electrolyte couple are shown in Figures 15 and 16, respectively.
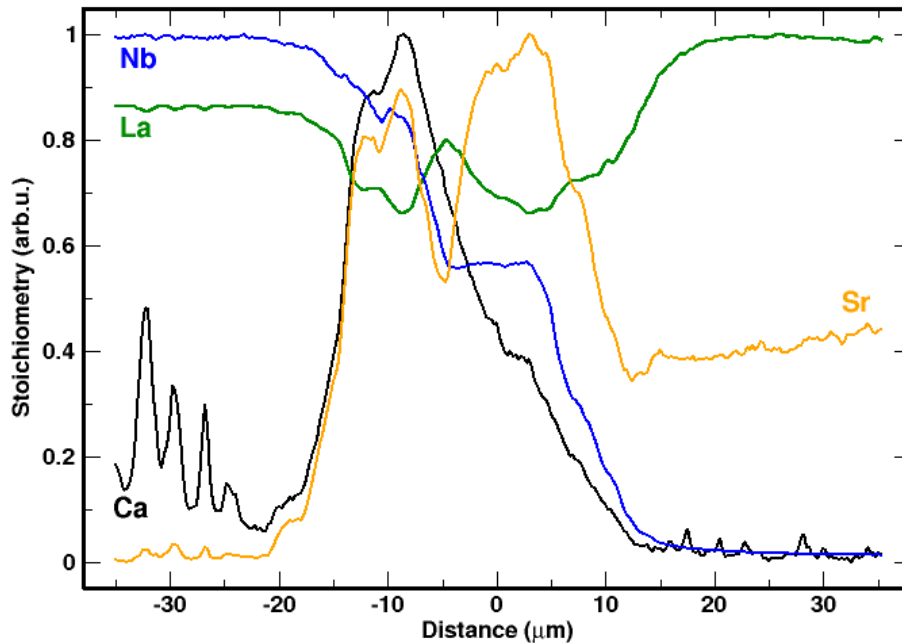
Figure 15 - LSC/LNC 72h at the La L$_3$-edge. Concentration profiles of niobium (blue), calcium (black), lanthanum (green), and strontium (orange).

The profiles are broadly similar to the LSCF/LNC couple described above, with a reactivity zone 35 μm wide. As it was the case in the other couples as well, different interface layers can be identified here: closer to the LSC side, a strontium enrichment at the expense of lanthanum is evident, together with reasonably large niobium and calcium content; moving towards LNC, a thin lanthanum-rich layer is encountered before a second mixed-cation region, containing maximum concentrations of calcium and strontium, and relatively less lanthanum. In bulk LNC, localized calcium clumps are evident on the far left of the profiles. Interestingly, these clumps are accompanied by analogous increases in the (however low) strontium content, which has migrated from LSC to LNC.

The features identified in the cation profiles are more evident in the elemental maps reported in Figure 16. In particular, the secondary phase formed close to the LNC side is composed of areas with acicular shape, rich in Ca, Sr and Nb, and poor in La. The formation on the opposite side, close to LSC, is rich in Sr and Nb alone and composed of small particles very close to each other (contrary to the relatively high porosity of LSC): these two layers are separated by a thin La-rich layer. The correlations and anticorrelations between the large cations Ca^{2+}, Sr^{2+} and La^{3+}, competing for the same lattice sites in the different phases, are shown in Figure 17.
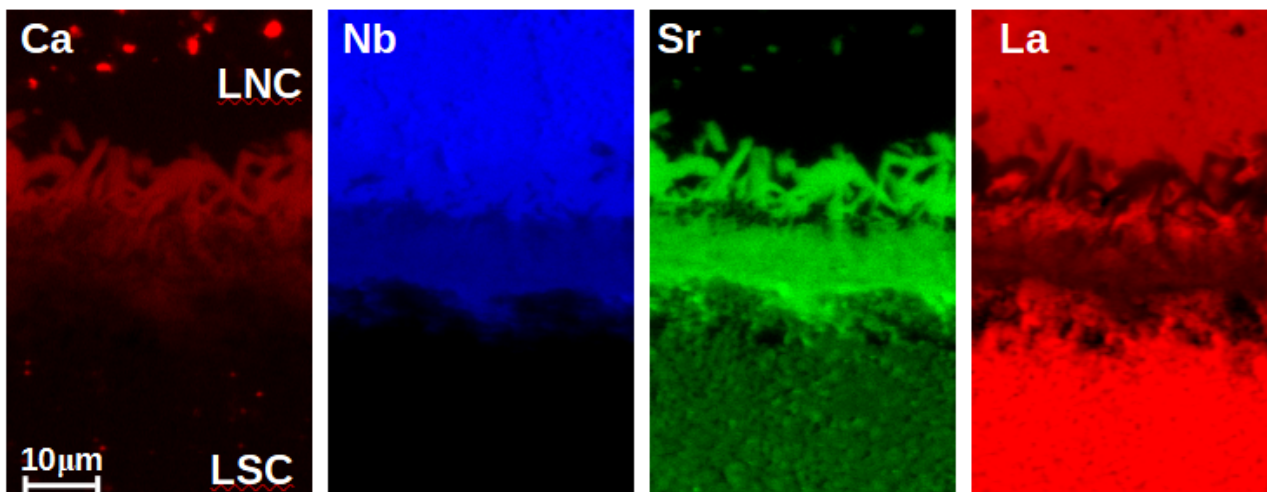
Figure 16 - LSC/LNC 72 h at the La L_3-edge. Left to right: concentration maps of calcium (red), niobium (blue), strontium (green), and lanthanum (red).
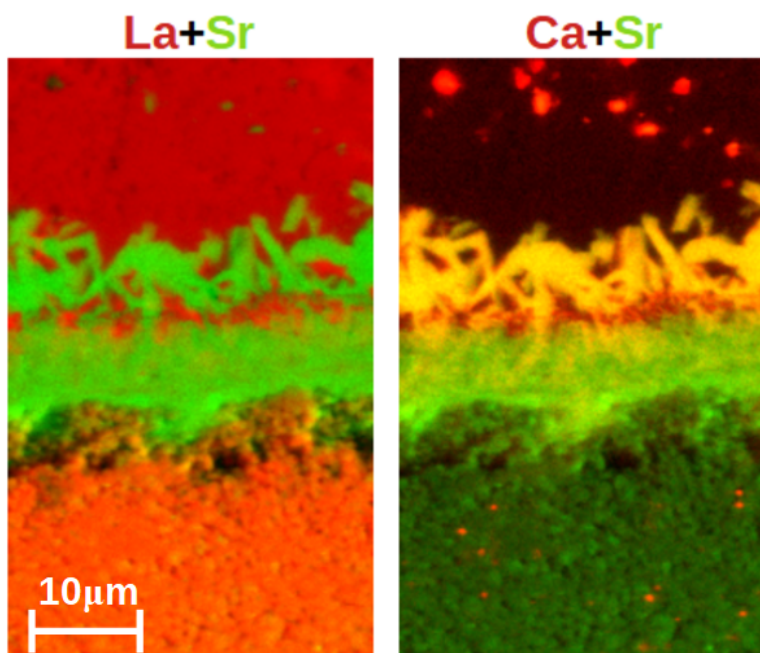

Figure 17 - LSC/LNC 72 h at the La L_3-edge. Left: correlation map of lanthanum (red) and strontium (green). Right: correlation map of calcium (red) and strontium (green).

The microXANES acquired at the Nb L_3-edge for the LSC/LNC bilayer are reported in Figure 18. Also, in this case, the absorption edge features show dramatic changes, indicating modified local environments for niobium, starting from LNC to the several secondary phases and eventually inside LSC.

Again, ab initio simulations were performed to model the local environment of niobium (Figure 19). In LNC, niobium is present as Nb^{5+} in a tetrahedral coordination. As it diffuses out of LNC towards the cathode, niobium is incorporated in a Nb:LSC phase where Nb^{5+}

substitutes cobalt in the B-site of the perovskite, then a $(Sr,Ca)_2Nb_2O_7$ layered perovskite phase is formed. Nb^{5+} features a conspicuous splitting of the main absorption edge in the two latter cases, typical of an octahedral environment (common to both LSC and $(Sr,Ca)_2Nb_2O_7$).
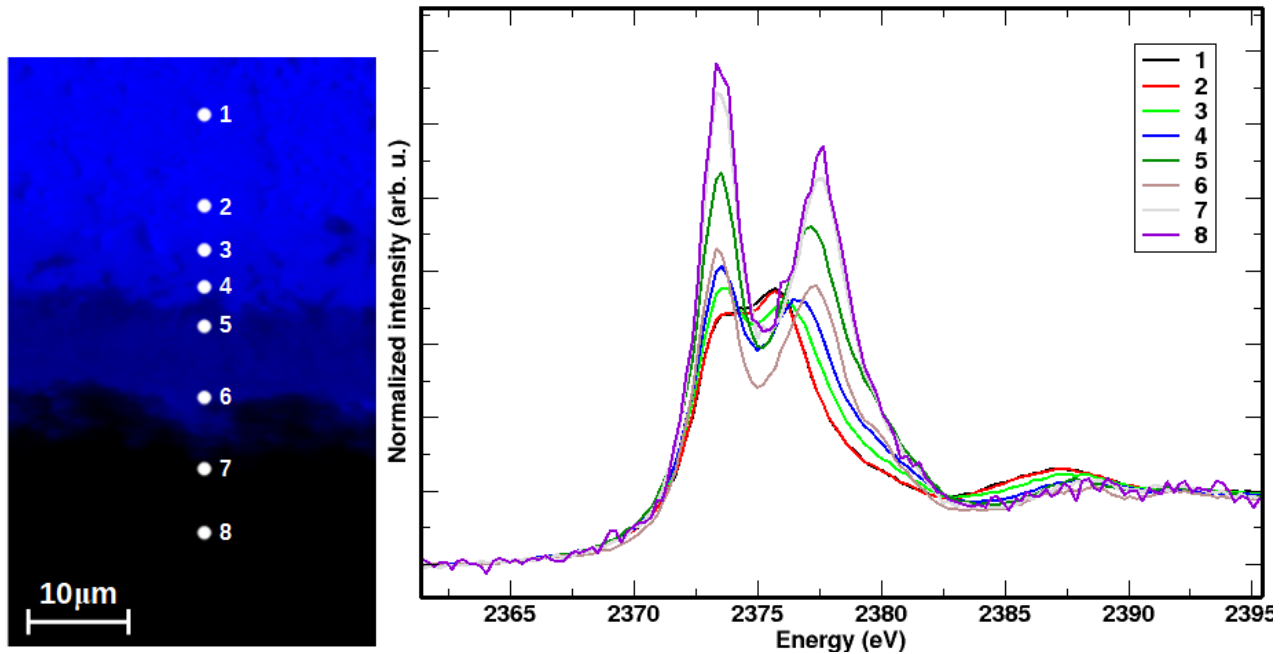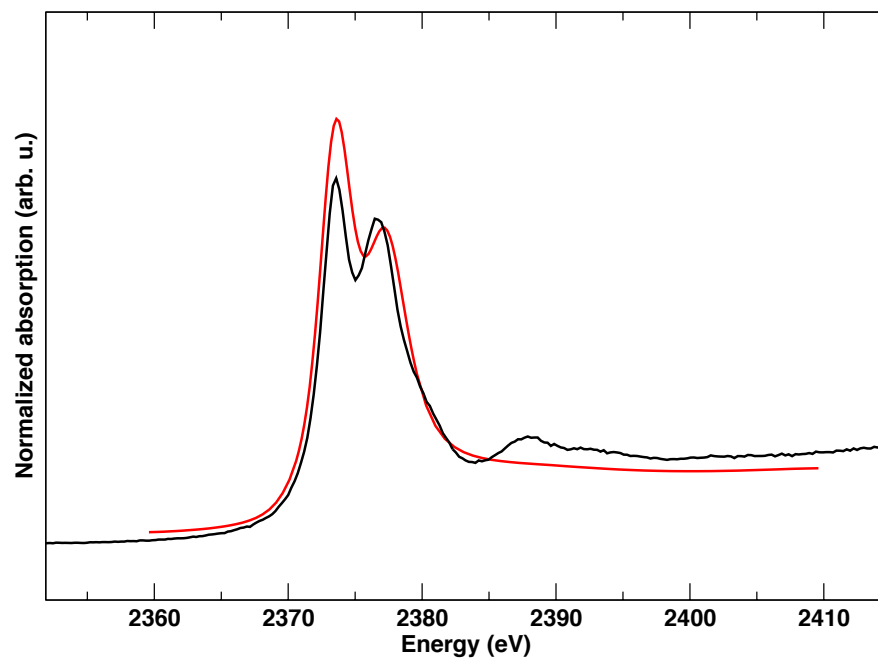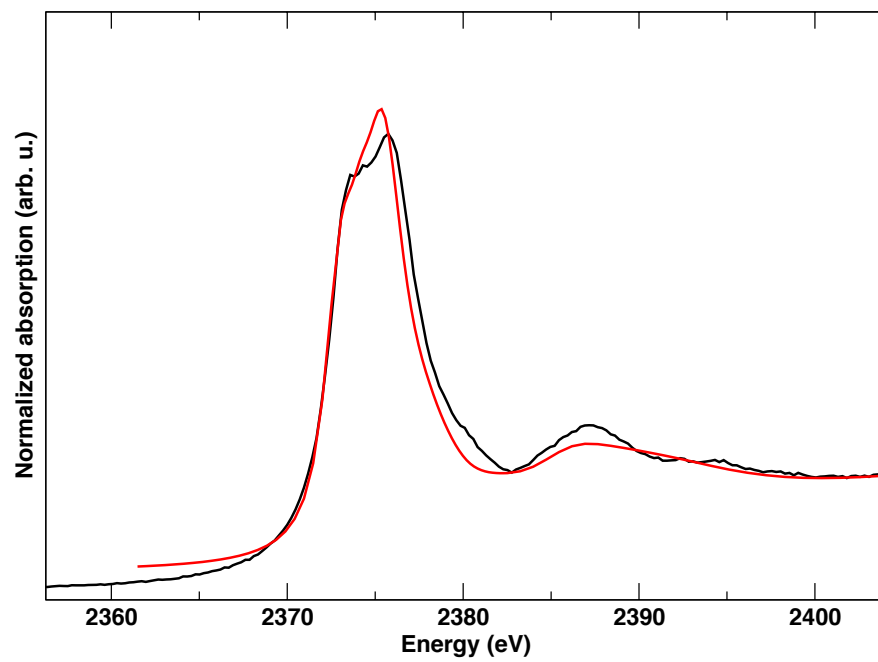

Figure 18 - LSC/LNC 72 h at the Nb L_3-edge. (Left) concentration map of niobium (blue). (Right) Nb L_3-edge microXANES spectra measured at different points shown in the left panel.
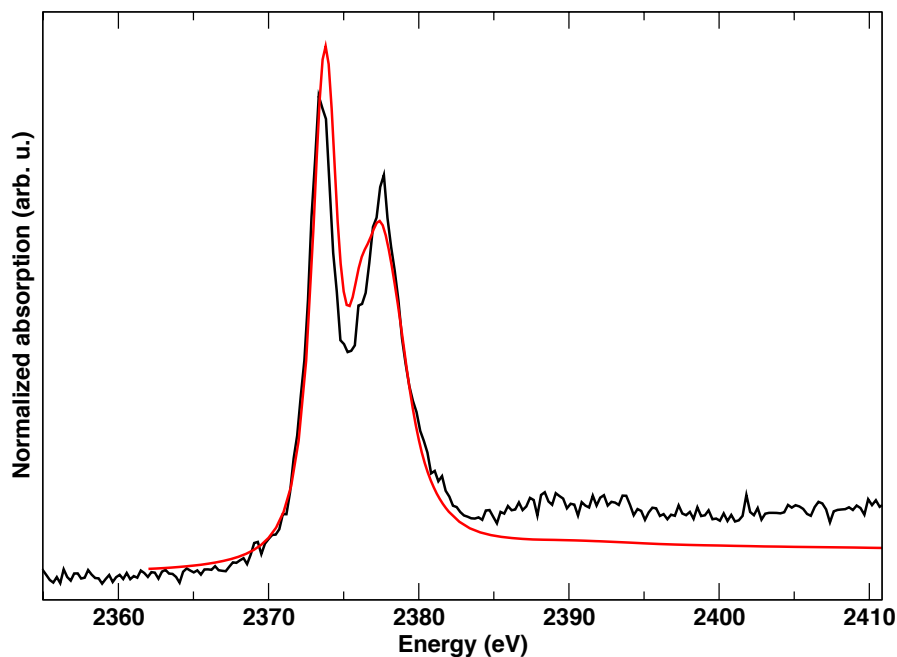
Figure 19 – LSC/LNC 72 h. Nb L_3-edge microXANES spectra (black) measured in spot 1 (top), spot 4 (middle), and spot 8 (bottom), together with the modeled spectra (red): the modeled spectra are calculated for Nb^{5+} in LNC (spot 1), Nb^{5+} in the B-site of LSC (spot 4), and Nb^{5+} in $Sr_2Nb_2O_7$ (spot 8).

Overall, although the reactivity observed in the LSC/LNC couple is similar to LSCF/LNC (as can be expected from their composition), the interface morphology is very different. In LSCF/LNC, the cation diffusion results in smooth profiles perpendicular to the interface, as expected in a concentration-driven process. On the other hand, cation migration from LSC drives the formation of needle-like crystals, which suggests the preferential diffusion of cations along these directions.

4. Conclusions

A comprehensive investigation of the solid-state reactivity between Ca-doped lanthanum niobate with perovskite cathodes was carried out using X-ray absorption microspectroscopy and ab initio modeling of the absorption spectra. The high-temperature treatments result in an evident cathode/electrolyte reactivity forming several secondary phases for all samples. In general, secondary phases are organized in layers parallel to the cathode/electrolyte

interface. Two major secondary phases were observed in all cases: one at the cathode side, with a structure and composition similar to the cathode but with a strong strontium enrichment; the other at the electrolyte side, with a perovskite-like $(Ca,Sr)_2Nb_2O_7$ structure. Despite all samples showing reactivity, the extent of the reactivity zone in the LSFCu/LNC couple is about three times larger than in the other two. In a previous study, the LSFCu and LSCF reactivity with trivalent-doped ceria was compared, finding similarly increased reactivity for the Cu-containing perovskite [31]. It seems evident that the presence of copper plays a role in the interface stability, triggering a faster interdiffusion.

Other significant differences are evident in the interface morphology. LSFCu/LNC and LSCF/LNC show a homogeneous cation distribution at the interface, while in LSC/LNC the needle-like secondary growth was identified as $(Ca,Sr)_2Nb_2O_7$. Although to a lesser extent than copper, cobalt increases the reactivity compared to an undoped $LaFeO_3$ which was found to be stable in contact with lanthanum niobate at high temperature [15].

Comparing the microXANES of all samples, each cation is found to follow a distinctive trend. Iron features an octahedral perovskite B-site environment in all the investigated zones, shifting to higher oxidation states inside the interface reactivity zone. The shift is driven by the higher strontium concentration present in the secondary phase, increasing Fe^{4+} content. In calcium microXANES spectra, it is possible to identify three different chemical environments: the first, inside bulk LNC, features Ca^{2+} in the La^{3+} site in the LNC lattice; the second is placed in the reactivity zone, and features calcium in the $(Ca,Sr)_2Nb_2O_7$ structure, together with $CaCO_3$; the third environment was identified in the cathode zone, and it is due to calcium entering the A-site of the perovskite cathode as a dopant. In the niobium microXANES, two chemical environments are found: one in bulk LNC, with Nb^{5+} tetrahedrally coordinated; in the reactivity zone, Nb^{5+} is present in both $(Ca,Sr)_2Nb_2O_7$ and as a dopant in the perovskite B-site.

In conclusion, the formation of secondary phases with various compositions and morphologies in the regions near the interface confirms the limited chemical compatibility between LNC electrolyte and LSCF/LSFCu cathodes. Among the cathode materials considered so far, LSM remains the most stable candidate. This study highlights the limited stability of lanthanum niobate against high-temperature treatments in contact with common perovskite cathodes, pointing out a severe issue in the long-term performance of SOFC devices based on these couples. Moreover, as previously put forward [8,12, 19,20,31], X-ray microprobe techniques are essential for assessing the solid-state compatibility in durable solid-state devices.

References

[1] S. Hossain, A.M. Abdalla, S.N.B. Jamain, J.H. Zaini, A.K. Azad, A review on proton conducting electrolytes for clean energy and intermediate temperature-solid oxide fuel cells, Renew. Sustain. Energy Rev. 79 (2017) 750–764. https://doi.org/10.1016/j.rser.2017.05.147.

[2] H.-I. Ji, J.-H. Lee, J.-W. Son, K.J. Yoon, S. Yang, B.-K. Kim, Protonic ceramic electrolysis cells for fuel production: a brief review, J. Korean Ceram. Soc. 57 (2020) 480–494. https://doi.org/10.1007/s43207-020-00059-4.

[3] M. Marrony, Proton-Conducting Ceramics: From Fundamentals to Applied Research, 0 ed., Jenny Stanford Publishing, 2015. https://doi.org/10.1201/b18921.

[4] K.D. Kreuer, Proton-Conducting Oxides, Annu. Rev. Mater. Res. 33 (2003) 333–359. https://doi.org/10.1146/annurev.matsci.33.022802.091825.

[5] K. Singh, R. Kannan, V. Thangadurai, Perspective of perovskite-type oxides for proton conducting solid oxide fuel cells, Solid State Ion. 339 (2019) 114951–114964. https://doi.org/10.1016/j.ssi.2019.04.014.

[6] S. Ricote, N. Bonanos, A. Manerbino, N.P. Sullivan, W.G. Coors, Effects of the fabrication process on the grain-boundary resistance in $BaZr_{0.9}Y_{0.1}O_{3-\delta}$, J. Mater. Chem. A. 2 (2014) 16107–16115. https://doi.org/10.1039/C4TA02848A.

[7] D.A. Medvedev, J.G. Lyagaeva, E.V. Gorbova, A.K. Demin, P. Tsiakaras, Advanced materials for SOFC application: Strategies for the development of highly conductive and stable solid oxide proton electrolytes, Prog. Mater. Sci. 75 (2016) 38–79. https://doi.org/10.1016/j.pmatsci.2015.08.001.

[8] A. Chiara, F. Giannici, C. Pipitone, A. Longo, C. Aliotta, M. Gambino, A. Martorana, Solid–Solid Interfaces in Protonic Ceramic Devices: A Critical Review, ACS Appl. Mater. Interfaces. 12 (2020) 55537–55553. https://doi.org/10.1021/acsami.0c13092.

[9] L. Lei, Z. Tao, X. Wang, J.P. Lemmon, F. Chen, Intermediate-temperature solid oxide electrolysis cells with thin proton-conducting electrolyte and a robust air electrode, J. Mater. Chem. A. 5 (2017) 22945–22951. https://doi.org/10.1039/C7TA05841A.

[10] P.S. Mahadik, A.N. Shirsat, B. Saha, N. Sitapure, D. Tyagi, S. Varma, B.N. Wani, S.R. Bharadwaj, Chemical compatibility study of BSCF cathode materials with proton-conducting BCY/BCZY/BZY electrolytes, J. Therm. Anal. Calorim. 137 (2019) 1857–1866. https://doi.org/10.1007/s10973-019-08082-2.

[11] J. Lyagaeva, D. Medvedev, E. Pikalova, S. Plaksin, A. Brouzgou, A. Demin, P. Tsiakaras, A detailed analysis of thermal and chemical compatibility of cathode materials suitable for $BaCe_{0.8}Y_{0.2}O_{3-\delta}$ and $BaZr_{0.8}Y_{0.2}O_{3-\delta}$ proton electrolytes for solid oxide fuel cell application, Int. J. Hydrog. Energy. 42 (2017) 1715–1723. https://doi.org/10.1016/j.ijhydene.2016.07.248.

[12] F. Giannici, A. Chiara, G. Canu, A. Longo, A. Martorana, Interface Solid-State Reactions in $La_{0.8}Sr_{0.2}MnO_3/Ce_{0.8}Sm_{0.2}O_2$ and $La_{0.8}Sr_{0.2}MnO_3/BaCe_{0.9}Y_{0.1}O_3$ Disclosed by X-ray Microspectroscopy, ACS Appl. Energy Mater. 2 (2019) 3204–3210. https://doi.org/10.1021/acsaem.9b00037.

[13] L. Zhang, G. Chen, R. Dai, X. Lv, D. Yang, S. Geng, A review of the chemical compatibility between oxide electrodes and electrolytes in solid oxide fuel cells, J. Power Sources. 492 (2021) 229630–229649. https://doi.org/10.1016/j.jpowsour.2021.229630.

[14] R. Haugsrud, T. Norby, Proton conduction in rare-earth ortho-niobates and ortho-tantalates, Nature Mater. 5 (2006) 193–196. https://doi.org/10.1038/nmat1591.

[15] J.R. Tolchard, H.L. Lein, T. Grande, Chemical compatibility of proton conducting LaNbO4 electrolyte with potential oxide cathodes, J. Eur. Ceram. Soc. 29 (2009) 2823–2830. https://doi.org/10.1016/j.jeurceramsoc.2009.03.034.

[16] G. Canu, V. Buscaglia, C. Ferrara, P. Mustarelli, S. Gonçalves Patrício, A.I. Batista Rondão, C. Tealdi, F.M.B. Marques, Oxygen transport and chemical compatibility with electrode materials in scheelite-type $LaW_xNb_{1-x}O_{4+x/2}$ ceramic electrolyte, Journal of Alloys and Compounds. 697 (2017) 392–400. https://doi.org/10.1016/j.jallcom.2016.12.111.

[17] K.V. Kravchyk, E. Quarez, C. Solís, J.M. Serra, O. Joubert, Cathode materials for $La_{0.995}Ca_{0.005}NbO_4$ proton ceramic electrolyte, International Journal of Hydrogen Energy. 36 (2011) 13059–13066. https://doi.org/10.1016/j.ijhydene.2011.07.069.

[18] A. Magrasó, M.-L. Fontaine, R. Bredesen, R. Haugsrud, T. Norby, Cathode compatibility, operation, and stability of LaNbO4-based proton conducting fuel cells, Solid State Ion. 262 (2014) 382–387. https://doi.org/10.1016/j.ssi.2013.12.009.

[19] F. Giannici, G. Canu, M. Gambino, A. Longo, M. Salomé, M. Viviani, A. Martorana, Electrode–Electrolyte Compatibility in Solid-Oxide Fuel Cells: Investigation of the LSM–LNC Interface with X-ray Microspectroscopy, Chem. Mater. 27 (2015) 2763–2766. https://doi.org/10.1021/acs.chemmater.5b00142.

[20] G. Canu, F. Giannici, A. Chiara, G. Confalonieri, A. Longo, M.T. Buscaglia, M. Dapiaggi, V. Buscaglia, A. Martorana, Characterisation of scheelite $LaW_{0.16}Nb_{0.84}O_{4.08}$ ion conductor by combined synchrotron techniques: Structure, W oxidation state and interdiffusion, J. Alloys Compd. 857 (2021) 157532–157538. https://doi.org/10.1016/j.jallcom.2020.157532.

[21] T. Miruszewski, P. Winiarz, K. Dzierzgowski, K. Wiciak, K. Zagórski, A. Morawski, A. Mielewczyk-Gryń, S. Wachowski, J. Strychalska-Nowak, M. Sawczak, M. Gazda, Synthesis, microstructure and electrical properties of nanocrystalline calcium doped lanthanum orthoniobate, J. Solid State Chem. 270 (2019) 601–607. https://doi.org/10.1016/j.jssc.2018.12.034.

[22] M. Li, R. Wu, L. Zhu, J. Cheng, T. Hong, C. Xu, Enhanced sinterability and conductivity of cobalt doped lanthanum niobate as electrolyte for proton-conducting solid oxide fuel cell, Ceram. Int. 45 (2019) 573–578. https://doi.org/10.1016/j.ceramint.2018.09.210.

[23] X. Chi, Z. Wen, J. Zhang, Y. Liu, Enhanced conductivity of lanthanum niobate proton conductor by A and B-site co-doping: Synthesis, phase, microstructure and transport properties, Solid State Ion. 268 (2014) 326–329. https://doi.org/10.1016/j.ssi.2014.06.013.

[24] L. Bi, E. Fabbri, E. Traversa, Solid oxide fuel cells with proton-conducting $La_{0.99}Ca_{0.01}NbO_4$ electrolyte, Electrochim. Acta. 260 (2018) 748–754. https://doi.org/10.1016/j.electacta.2017.12.030.

[25] S. Wachowski, B. Kamecki, P. Winiarz, K. Dzierzgowski, A. Mielewczyk-Gryń, M. Gazda, Tailoring structural properties of lanthanum orthoniobates through an isovalent substitution on the Nb-site, Inorg. Chem. Front. 5 (2018) 2157–2166. https://doi.org/10.1039/C8QI00524A.

[26] M. Salomé, M. Cotte, R. Baker, R. Barrett, N. Benseny-Cases, G. Berruyer, D. Bugnazet, H. Castillo-Michel, C. Cornu, B. Fayard, E. Gagliardini, R. Hino, J. Morse, E. Papillon, E. Pouyet, C. Rivard, V.A. Solé, J. Susini, G. Veronesi, The ID21 Scanning X-ray

Microscope at ESRF, J. Phys.: Conf. Ser. 425 (2013) 182004–182008. https://doi.org/10.1088/1742-6596/425/18/182004.

[27] V.A. Solé, E. Papillon, M. Cotte, Ph. Walter, J. Susini, A multiplatform code for the analysis of energy-dispersive X-ray fluorescence spectra, Spectrochim. Acta B. 62 (2007) 63–68. https://doi.org/10.1016/j.sab.2006.12.002.

[28] Available at https://github.com/woutdenolf/spectrocrunch, n.d.

[29] O. Bunău, Y. Joly, Self-consistent aspects of x-ray absorption calculations, J. Phys.: Condens. Matter. 21 (2009) 345501–345512. https://doi.org/10.1088/0953-8984/21/34/345501.

[30] S.A. Guda, A.A. Guda, M.A. Soldatov, K.A. Lomachenko, A.L. Bugaev, C. Lamberti, W. Gawelda, C. Bressler, G. Smolentsev, A.V. Soldatov, Y. Joly, Optimized Finite Difference Method for the Full-Potential XANES Simulations: Application to Molecular Adsorption Geometries in MOFs and Metal–Ligand Intersystem Crossing Transients, J. Chem. Theory Comput. 11 (2015) 4512–4521. https://doi.org/10.1021/acs.jctc.5b00327.

[31] F. Giannici, G. Canu, A. Chiara, M. Gambino, C. Aliotta, A. Longo, V. Buscaglia, A. Martorana, Cation Diffusion and Segregation at the Interface between Samarium-Doped Ceria and LSCF or LSFCu Cathodes Investigated with X-ray Microspectroscopy, ACS Appl. Mater. Interfaces. 9 (2017) 44466–44477. https://doi.org/10.1021/acsami.7b13377.

[32] T. Mokkelbost, I. Kaus, R. Haugsrud, T. Norby, T. Grande, M.-A. Einarsrud, High-Temperature Proton-Conducting Lanthanum Ortho-Niobate-Based Materials. Part II: Sintering Properties and Solubility of Alkaline Earth Oxides, J. Am. Ceram. Soc. 91 (2008) 879–886. https://doi.org/10.1111/j.1551-2916.2007.02232.x.

[33] G.E. Syvertsen, A. Magrasó, R. Haugsrud, M.-A. Einarsrud, T. Grande, The effect of cation non-stoichiometry in LaNbO4 materials, Int. J. Hydrog. Energy. 37 (2012) 8017–8026. https://doi.org/10.1016/j.ijhydene.2011.10.113.

[34] S. Sønderby, P.L. Popa, J. Lu, B.H. Christensen, K.P. Almtoft, L.P. Nielsen, P. Eklund, Strontium Diffusion in Magnetron Sputtered Gadolinia-Doped Ceria Thin Film Barrier Coatings for Solid Oxide Fuel Cells, Adv. Energy Mater. 3 (2013) 923–929. https://doi.org/10.1002/aenm.201300003.

[35] F. Wang, M. Nishi, M.E. Brito, H. Kishimoto, K. Yamaji, H. Yokokawa, T. Horita, Sr and Zr diffusion in LSCF/10GDC/8YSZ triplets for solid oxide fuel cells (SOFCs), J. Power Sources. 258 (2014) 281–289. https://doi.org/10.1016/j.jpowsour.2014.02.046.

[36] A. Saito, H. Kagi, S. Marugata, K. Komatsu, D. Enomoto, K. Maruyama, J. Kawano, Incorporation of Incompatible Strontium and Barium Ions into Calcite ($CaCO_3$) through

Amorphous Calcium Carbonate, Minerals. 10 (2020) 270–283. https://doi.org/10.3390/min10030270.

[37] D.J. Cherniak, An experimental study of strontium and lead diffusion in calcite, and implications for carbonate diagenesis and metamorphism, Geochim. Cosmochim. Acta. 61 (1997) 4173–4179. https://doi.org/10.1016/S0016-7037(97)00236-6.